Hybrid fiber/bulk laser source designed for CO 2 and wind measurements at 2.05 μm

Julien Lahyani, Mathys Thiers, Fabien Gibert, Dimitri Edouart, Julien Le Gouët, Nicolas Cézard

Optics Letters

Hybrid fiber/bulk laser source designed for CO_2 and wind measurements at 2.05 µm

Julien Lahyani,[1,*] Mathys Thiers,[1,2] Fabien Gibert,[2] Dimitri Edouart,[2] Julien Le Gouët,[1] and Nicolas Cézard[3]

[1]DOTA, ONERA, Université Paris-Saclay, F-91123 Palaiseau, France
[2]LMD/CNRS, Ecole Polytechnique, F-91123 Palaiseau Cedex, France
[3]ONERA/DOTA, Université de Toulouse, F-31055 Toulouse, France
*julien.lahyani@onera.fr

Received 2 November 2023; revised 21 December 2023; accepted 13 January 2024; posted 19 January 2024; published 12 February 2024

We present a hybrid fiber/bulk laser source designed for CO_2 and wind monitoring using differential absorption LIDAR (DIAL) and coherent detection at 2.05 µm. This source features a master oscillator power amplifier (MOPA) architecture made of four fiber stages and one single-pass, end-pumped, bulk amplifier. This Letter focuses on the single-pass bulk amplifier performance and on the hybrid architecture benefits for DIAL and coherent detection. The bulk material is a holmium-doped YLF crystal that provides high efficiency amplification at 2.05 µm. This laser offers an energy breakthrough as compared to the classical stimulated Brillouin scattering (SBS) limit encountered in a fiber laser without compromising robustness, thanks to very few free-space optical elements and a small optical path. It delivers pulse energy and repetition frequency of 9.0 or 1.2 mJ/20 kHz with 200 ns quasi Fourier-transform limited pulses.

https://doi.org/10.1364/OL.510598

Carbon dioxide (CO_2) is widely acknowledged as the most important anthropogenic greenhouse gas in the atmosphere. Its measurement, at a global scale, is essential to better understand its impact on climate change. Local scale monitoring is also of interest to study the dynamics of CO_2 in the boundary layer and characterize natural and anthropogenic sources and sinks.

Differential absorption LIDAR (DIAL) can provide continuous CO_2 measurement profiles and/or 3D maps at different spatial scales with very small bias together with flux estimation when associated with wind speed measurement (e.g. using coherent detection) [1]. DIAL application requires stringent laser performance, such as narrow linewidth and high energy, combined with high robustness for operational use.

Many CO_2 DIAL systems include lasers at 1.57 or 2.05 µm due to well-suited absorption lines (suited cross section, low temperature dependence, low water vapor absorption interference, etc.).

These wavelengths are accessible by direct generation using erbium-doped fibers (1.57 µm) [2] or thulium/holmium-doped materials (fiber or crystal) (2.05 µm) [3–5] and by parametric generation (1.57 and 2.05 µm) [6,7]. However, free-space oscillators generally require major mechanical development efforts to ensure operation in a vibrating environment, and fiber laser sources are generally limited in terms of peak power by stimulated Brillouin scattering (SBS). The robustness of the system and the SBS represent limitations commonly encountered in field deployment and measurement accuracy/range respectively.

The laser design presented in this Letter features a master oscillator power amplifier (MOPA) architecture using the all-fiber MOPA described in [8] followed by a single-pass bulk amplifier. The resulting hybrid source combines the robustness of the fiber architecture and the high peak power reachable in the bulk material. Regarding DIAL application requirements, this architecture facilitates multi-wavelength operation, which is an additional challenge for a seeded cavity as explained in [9]. Furthermore, this architecture is well suited to coherent detection, as it eases the spectral single-mode operation and reduces the frequency jitter encountered in [9] due to imperfect resonance. It will thus permit a straightforward simultaneous estimation of wind and gas concentration with a single LIDAR instrument, which is the major strength for flux measurement.

The hybrid architecture is shown in Fig. 1. It features two seeders, called λ_{on} and λ_{off}, associated with an optical switch (OS) to perform a sequential measurement on and off the targeted absorption line. The fibered amplification chain is made of one continuous wave amplifier and three pulsed amplifiers [8].

The free-space amplifier is made of a Ho:YLF crystal, pumped by a commercial single-transverse-mode Tm-doped fiber laser oscillator (model TLR-50-AC from IPG Photonics) and randomly polarized, which can deliver up to 50 W of continuous wave at 1940 nm. The pump laser system provides a collimated beam with a diameter of 5.9 mm and an M^2 figure of 1.1 according to the constructor's information. The use of a YLF lattice is motivated by several criteria: highest emission cross section at 2.05 µm [10], long lifetime of the upper-state level [11], and low upconversion parameter as compared to the other main lattices [12]; all parameters are in favor of the amplification efficiency.

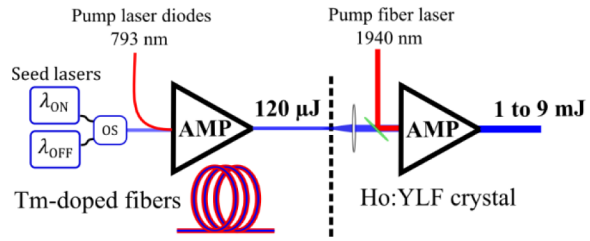

Fig. 1. Schematic of the hybrid laser. OS, optical switch, and the dotted vertical line represents the fiber/free-space interface.

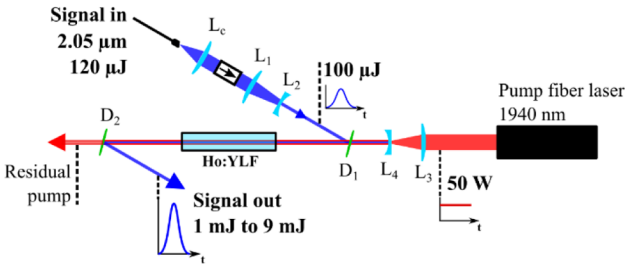

Fig. 2. Schematic of the bulk amplifier setup. L denotes lenses, D dichroic plates, and the arrow in the box an optical isolator. Focal lengths: $L_c = 18$ mm, $L_1 = 75$ mm, $L_2 = -50$ mm, $L_3 = 150$ mm, and $L_4 = -30$ mm.

The amplification is based on a single-pass co-propagative end-pumped scheme. The experimental scheme of the bulk amplifier is given in Fig. 2.

The output of the preamplifier is collimated by the lens *Lc* and isolated to protect it from backreflections. The L_1/L_2 and L_3/L_4 lens pairs focus the signal and pump beams into the crystal once combined by the D_1 dichroic plate. The dichroic plates are anti-reflection coated at 1.94 µm (reflection <0.2%) and provide high reflectivity at 2.05 µm (>99.9%) on both polarizations. In the crystal, the signal and pump beams are overlapped and have the same diameter of 600 µm. The crystal is a-cut, 13 cm-long, 5 mm-wide (cylindrical), 0.5 at. % holmium-doped, anti-reflection coated at pump and signal wavelengths, and water cooled. The D_2 plate separates the signal and the pump. Since the YLF lattice is birefringent, special attention was paid to align the signal polarization on the π axis to maintain the linear polarization and take advantage of a higher emission cross section than on the σ axis [11]. The random polarization of the pump beam leads to a slightly lower pulse energy than with a polarized laser (around 10% difference in signal output pulse energy for the same pump power according to the simulation described below). The main features of the complete laser architecture are summarized in Table 1.

In our previous work on the preamplifier [8], all characterizations were carried out at a pulse repetition frequency (PRF) of 20 kHz, as this is an optimal operating point for the fiber laser (low amplified spontaneous emission (ASE) production). Here we further assess how the PRF influences the overall architecture performance and compare experimental results with the simulation.

Changing the PRF is simply achieved since it is ruled by the PRF of the voltage drive applied to the acousto-optic modulator (AOM) in the preamplifier. However, the pump power in this stage must be adjusted to keep the peak power below the

Table 1. Main Laser Features

Features	Result in This Study	
Amplification media	Tm:fiber–Ho:YLF	
Laser wavelength	2051 nm	
Spectral tunability	2 nm	
PRF	1 kHz	20 kHz
Pulse energy	9.0 mJ	1.2 mJ
Peak—average power	45 kW/9 W	6 kW/24 W
Pulse duration	187 ns	200 ns
	(quasi FT-limited)	
Electro-optic eff.	2.7%	6.5%
M^2	≤1.2	

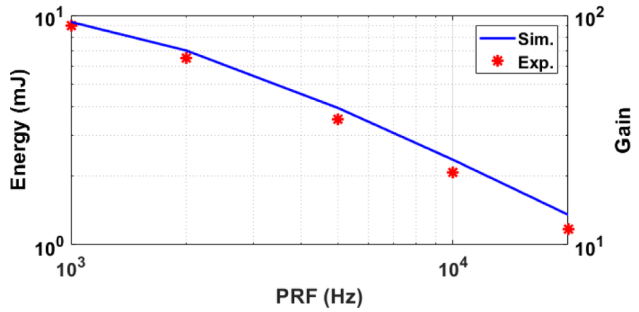

Fig. 3. Simulation (blue line) and experimental results (red dots) comparison of the pulse energy versus the PRF for the seeding energy of 100 µJ and 50 W crystal pump power.

SBS limit. The only notable PRF effect on the preamplifier performance is an increase in the ASE proportion at lower PRF as expected (some details are given below). A major part of this ASE is subsequently attenuated due to the Ho^{3+} absorption in the crystal (absorbed ASE does not play an important role in the amplification process) and to the dichroic plates. During our tests, the preamplifier output pulse energy/duration was maintained at 120 µJ/200 ns without difficulty for the PRF ranging from 20 kHz down to 1 kHz. At the crystal input, the signal energy is 100 µJ (approx. 12% transmission losses from the isolator and 6% from lenses L_c, L_1, and L_2).

In contrast to the preamplifier, the bulk stage can be pumped at the same power regardless of the PRF (no SBS limit). Due to the continuous pumping regime, the amplified signal energy in the crystal strongly varies with the PRF: the lower the PRF, the longer the pumping duration and the higher the population inversion. Figure 3 shows the pulse energy (left axis) and the gain (linear, right axis) versus the PRF obtained at the output of the crystal amplifier, as well as the simulation results (described below).

At a PRF of 20 kHz, the signal energy is 1.2 mJ, which corresponds to a gain of 10 dB compared to the preamplifier output. The absorbed pump power is 39.5 W. When reducing the PRF to 1 kHz, the pulse energy reaches 9.0 mJ, corresponding to a gain of 19 dB, while the absorbed pump power decreases to 28.5 W. At this PRF, the peak power is 45 kW, while it is limited to 0.8 kW in the preamplifier. The hybrid fiber-bulk architecture therefore shows a significant advantage over an all-fiber SBS-limited architecture, and the robustness is not severely jeopardized. Regarding the pulse duration, it remains 200 ns at a PRF of 20 kHz. We observed a small distortion at low PRFs which leads to shorter pulses, 187 ns at 1 kHz.

Table 2. Relevant Parameters for Ho:YLF Amplification Simulation Found in Literature at Room Temperature

Crystal Axis	π	σ
Cross sections (λ) [11]		
Abs. (1940 nm)	1.00^{-20} cm^2	$0.36{\cdot}10^{-20}$ cm^2
Em. (1940 nm)	$0.77{\cdot}10^{-20}$ cm^2	$0.25{\cdot}10^{-20}$ cm^2
Abs. (2051 nm)	$0.50{\cdot}10^{-20}$ cm^2	Not used
Em. (2051 nm)	$1.50{\cdot}10^{-20}$ cm^2	Not used
τ_7 [11]	14 ms	
P_{77} [12]	$3.2{\cdot}10^{-24}$ m^3/s *(for 2 at. % Ho^{3+} doping level)*	

In order to help understand the experimental results and the design of future laser or LIDAR systems, we developed a numerical simulation. Amplification with Ho^{3+} around 2.05 µm uses the transition $^5I_7 \rightarrow {}^5I_8$. The rate equation that describes the amplification process can be expressed as [12]

$$\frac{dN_7}{dt} = -\frac{N_7}{\tau_7} - P_{77}N_7^2 + \frac{d\phi_P}{dz} - \frac{d\phi_S}{dz}, \quad (1)$$

where N_7 is the ion density in the $^5I_7$ manifold (m^{-3}), τ_7 is the $^5I_7$ manifold lifetime (s), P_{77} is the upconversion energy-transfer parameter for the Ho^{3+} $^5I_7$ manifold (m^3/s), ϕ_P and ϕ_S are the photon flux of the pump and the signal (m$^{-2}{\cdot}$s^{-1}), respectively. A summary of the values found in the literature is given in Table 2.

The cross section parameters (absorption and emission on π and σ axes) are taken from [11] as well as the $^5I_7$ level lifetime. The upconversion parameter indicated in [12] is $3.2{\cdot}10^{-24}$ m^3/s for a holmium concentration of 2 at. %. Considering the quadratic dependency reported in [13] for the upconversion parameter at low concentration, we assume a value of P_{77} divided by factor 16 for our 0.5 at. % doping level.

Our simulation is based on the model described in [12], with some approximations to simplify numerical calculations. In particular, the beams are considered collimated all along the crystal length (valid when the confocal parameter is longer than the crystal length), and thermal effects are omitted (cross section variations with temperature and thermal lensing). In our case, the confocal parameter is about 26 cm for a 13 cm-long crystal, so the first approximation seems valid. As for the thermal effects, Ref. [14] suggests that the Ho:YLF amplification is not subject to a significant cross section variation with a temperature within the range of intensities that we use. Nevertheless, we did not measure the temperature or estimate the thermal lens. Hence, our second approximation could have some influence on the simulation accuracy. Yet Fig. 3 shows a good agreement between the experiment and the simulation with less than 15% discrepancy.

For mobile LIDAR applications, the laser efficiency is generally a major concern. We compare here the electro-optic efficiency (EOE) of our laser source to previous studies. We define EOE as the signal optical power divided by the electrical consumption of the pump laser diodes. The electrical power consumption of cooling and driving systems is not included in the calculation. For a proper comparison, we consider the current state-of-the-art pump laser efficiencies as they represent the major source of electrical consumption. For the cavity oscillator using a Ho:YLF crystal presented in [9] at a PRF of 2 kHz, the EOE is 6% considering a 1.94 µm pump laser EOE of 20% [15]. For the frequency conversion-based oscillator described in [7] at a PRF of 100 Hz, the EOE is 2.4% considering a 1.06 µm Nd:YAG pump laser EOE of 12% [16]. In our architecture, the preamplifier's pump laser diodes' EOE is 50% and delivers 40 W at a PRF of 1 kHz and 60 W at 20 kHz. The 1.94 µm pump laser EOE is 20% and delivers 50 W optical power. The total electrical consumption is then 330 W at a PRF of 1 kHz and 370 W at 20 kHz. Considering the average output power reported in Table 1, it represents a global EOE of 2.7% at 1 kHz and 6.5% at 20 kHz. Therefore, the EOE of the hybrid architecture is comparable with respect to previously reported 2.05 µm sources for CO_2 LIDARs.

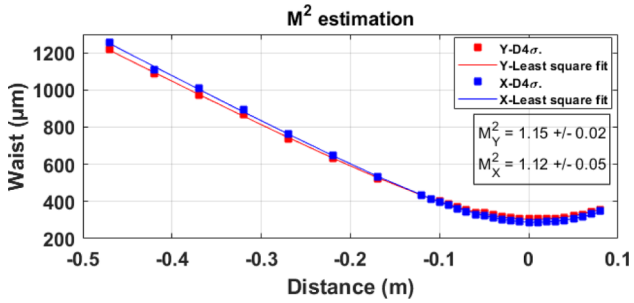

Fig. 4. Beam quality (M^2) at 1 kHz PRF.

We carefully checked that the free-space amplification does not affect the beam characteristics in terms of spatial and spectral quality, regardless the PRF. Consequently, the energy gain provided by the bulk stage is expected to fully translate into an effective LIDAR signal gain for coherent DIAL applications.

The measurement of the spatial quality (M^2) is shown in Fig. 4.

We find an M^2 lower than 1.2 for a PRF of 1 kHz and slightly better at 20 kHz (M^2 of 1.1). According to [17] it represents a degradation of the LIDAR signal carrier-to-noise ratio (in coherent detection) of 10–20%, which is significant and justifies how important the M^2 figure is for the coherent LIDAR purpose.

As for spectral quality, which is also of paramount importance for coherent detection and DIAL LIDAR applications, it has been assessed first using an optical spectrum analyzer (OSA) with 0.5 nm spectral resolution at the lowest PRF (1 kHz), which is the worst case for the continuously pumped amplifier (potentially high ASE fraction).

From the spectrum in Fig. 5, we find that the ASE represents about 20% of the preamplifier output power for a PRF of 1 kHz (blue curve) and that this figure drops to 0.2% at the crystal amplifier output (red curve). This was an unexpected but a beneficial effect of the Ho^{3+} absorption and dichroic plates that improves the spectral quality of the system at low PRF.

The spectral quality was analyzed in more detail by measuring the heterodyne beat note between small fractions of the emitted pulses with a local oscillator (LO). The signal is then detected with a fast photodiode at a 250 MHz sampling rate. The PSD and the pulse shape (simply measured by a photodiode) at the bulk amplifier's output (red curve) are compared with those at the preamplifier's output (blue curve) and show very close results.

The result is displayed in Fig. 6 (temporal shape on the left, spectral shape on the right). It shows that the temporal shape at the bulk amplifier output is slightly distorted due to the amplification [18] as compared to the preamplifier output. Nevertheless, it does not degrade the width of the PSD (right) which maintains at 3 MHz (Fourier-transform limit is 2.4 MHz for 187 ns Gaussian-shaped pulses).

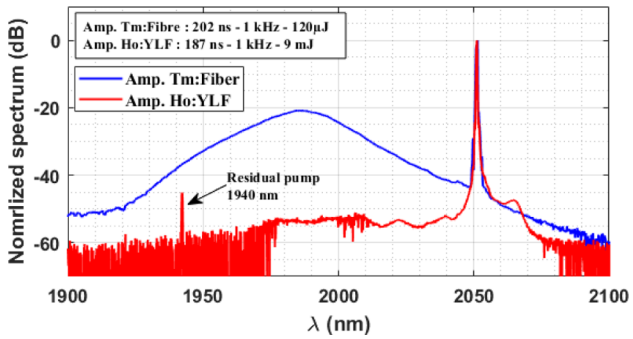

Fig. 5. Spectrum at the fiber laser output (blue) and at the bulk amplifier output (red) for a 1 kHz PRF.

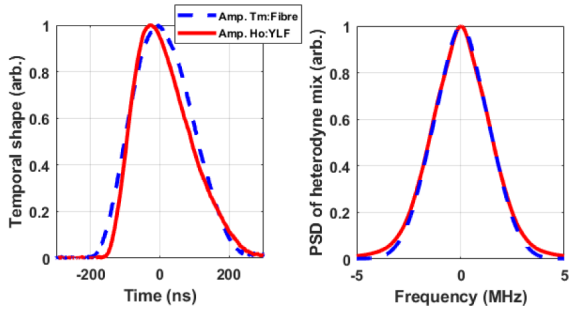

Fig. 6. Comparison of the temporal shape of the pulse (left) and the PSD calculated from the beat note with a LO (right) between the output of the fiber laser (dashed blue) and the bulk amplifier output (full red) for a 1 kHz PRF.

To summarize, we have proposed a hybrid MOPA architecture combining fiber and crystal amplification dedicated to DIAL measurements and coherent detection. As compared to the all-fiber architecture limited in terms of peak power by the SBS, this hybrid solution is able to deliver up to 90 times higher pulse energy (9.0 mJ) with a small pulse distortion (187 ns instead of 200 ns). The laser beam is quasi diffraction limited ($M^2 \leq 1.2$) and quasi Fourier-transform limited. The obtained energy is comparable to the previously reported laser source with oscillator-based direct generation [9] or frequency conversion [19] at 2.05 µm, but as compared to these previous results based on free-space oscillators, our hybrid amplifier architecture involves fewer free-space optical elements and only a single-pass alignment. This strongly alleviates (mis)alignment issues and mechanical tolerance for the field operation.

The hybrid architecture also permits to set quasi independently and easily several critical parameters like pulse duration, pulse shape, and PRF. This comes in contrast with previously reported architectures involving a cavity where the pumping rate/PRF and pulse duration were strongly dependent [9] or limited by the pump laser performance [6]. This hybrid source is therefore expected to be widely versatile and operable under a variety of settings optimized to various observation requirements (e.g. short pulse for high spatial resolution, high PRF for high temporal resolution, or high energy for long range measurement).

This work especially targets the CO_2 and wind measurement using the DIAL method combined with coherent detection for flux measurement. Nevertheless, this architecture is also suitable for direct detection and allows the simultaneous monitoring of H_2O using the absorption line located at 2050.5 nm.

Funding. Centre National d'Etudes Spatiales (190192, 5100018351); Office National d'études et de Recherches Aérospatiales (Atmosphère, ROSALI, TELEMAC).

Disclosures. Authors declare no conflicts of interest.

Data availability. Data underlying the results presented in this paper are not publicly available at this time but may be obtained from the authors upon reasonable request.

REFERENCES

1. F. Gibert, G. J. Koch, J. Y. Beyon, *et al.*, Atmospheric Ocean. Technol **28**, 365 (2011).
2. A. W. Yu, J. B. Abshire, M. Storm, *et al.*, in *Proc. SPIE* (2015), p. 9342.
3. E. Lucas, L. Lombard, Y. Jaouën, *et al.*, Appl. Opt. **53**, 4413 (2014).
4. J. Geng, Q. Wang, T. Luo, *et al.*, Opt. Lett. **37**, 3795 (2012).
5. G. J. Koch, J. Y. Beyon, F. Gibert, *et al.*, Appl. Opt. **47**, 944 (2008).
6. A. Amediek, A. Fix, M. Wirth, *et al.*, Appl. Phys. B **92**, 295 (2008).
7. J. Hamperl, J. F. Geus, K. M. Mølster, *et al.*, Atmosphere **12**, 402 (2021).
8. J. Lahyani, J. Le Gouët, F. Gibert, *et al.*, Appl. Opt. **60**, C12 (2021).
9. F. Gibert, D. Edouart, C. Cénac, *et al.*, Appl. Phys. B **116**, 967 (2014).
10. M. Eichhorn, Appl. Phys. B **93**, 269 (2008).
11. B. M. Walsh, N. P. Barnes, and B. Di Bartolo, J. Appl. Phys. **83**, 2772 (1998).
12. N. P. Barnes, B. M. Walsh, and E. D. Filer, J. Opt. Soc. Am. B **20**, 1212 (2003).
13. L. B. Shaw, R. S. F. Chang, and N. Djeu, Phys. Rev. B **50**, 6609 (1994).
14. E. Ji, Y. Shen, M. Nie, *et al.*, Appl. Phys. B **123**, 129 (2017).
15. T. S. McComb, R. A. Sims, C. C. C. Willis, *et al.*, Appl. Opt. **49**, 6236 (2010).
16. Z. Zhu, S. Lv, H. Zhang, *et al.*, Opt. Express **29**, 32325 (2021).
17. J.-P. Cariou, B. Augere, and M. Valla, Comptes Rendus Phys. **7**, 213 (2006).
18. L. M. Frantz and J. S. Nodvik, J. Appl. Phys. **34**, 2346 (1963).
19. E. Cadiou, D. Mammez, J.-B. Dherbecourt, *et al.*, Opt. Lett. **42**, 4044 (2017).